energies

*Article*

# Optimal Rotor Design for Reducing Electromagnetic Vibration in Traction Motors Based on Numerical Analysis

**Seung-Heon Lee [1], Si-Woo Song [2], In-Jun Yang [2], Ju Lee [2] and Won-Ho Kim [3,*]**

1 Department of Next Generation Energy System Convergence, Gachon University, Seongnam 461-701, Republic of Korea; dltmdgjs153@naver.com
2 Department of Electrical Engineering, Hanyang University, Seoul 133-791, Republic of Korea; thdtldn93@naver.com (S.-W.S.); dlswns78@naver.com (I.-J.Y.); julee@hanyang.ac.kr (J.L.)
3 Department of Electrical Engineering, Gachon University, Seongnam 461-701, Republic of Korea
* Correspondence: wh15@gachon.ac.kr; Tel.: +82-10-9856-1535

**Abstract:** Interior permanent magnet synchronous motor (IPMSM) for traction applications have attracted significant attention due to their advantages of high torque and power density as well as a wide operating range. However, these motors suffer from high electromagnetic vibration noise due to their complex structure and structural rigidity. The main sources of this electromagnetic vibration noise are cogging torque, torque ripple, and radial force. To predict electromagnetic vibration noise, finite element analysis (FEA) with flux density analysis of the air gap is essential. This approach allows for the calculation of radial force that is the source of the vibration and enables the prediction of vibration in advance. The data obtained from these analyses provide important guidance for reducing vibration and noise in the design of electric motors. In this paper, the cogging torque and vibration at rated and maximum operating speed are analyzed, and an optimal cogging torque and vibration reduction model, with rotor taper and two-step skew structure, is proposed using the response surface method (RSM) to minimize them. The validity of the proposed model is demonstrated through formulations and FEA based entirely on numerical analysis and results. This study is expected to contribute to the design of more efficient and quieter electric motors by providing a solution to the electromagnetic vibration noise problem generated by IPMSM for traction applications with complex structures.

**Keywords:** IPMSM; traction motor; noise; vibration; RSM; cogging torque; taper; two-step skew



**Citation:** Lee, S.-H.; Song, S.-W.; Yang, I.-J.; Lee, J.; Kim, W.-H. Optimal Rotor Design for Reducing Electromagnetic Vibration in Traction Motors Based on Numerical Analysis. *Energies* **2024**, *17*, 6206. https://doi.org/10.3390/en17236206

Academic Editor: Davide Astolfi

Received: 10 November 2024
Revised: 5 December 2024
Accepted: 7 December 2024
Published: 9 December 2024



## 1. Introduction

Increasing energy consumption and stricter environmental regulations around the world are driving the need for high-performance and efficient electric motors. Traction motors, in particular, require high torque and power density, and interior permanent magnet synchronous motor (IPMSM) models are the right choice to meet these needs. The pursuit of higher power density, lighter weight, and a wider speed range for traction compared to other applications presents the challenges of a more complex structure and lower structural rigidity, resulting in higher vibration and noise. Vibration and noise generated during operation in motors can hinder driver comfort and negatively affect the performance and lifetime of the motor [1–3]. Research to reduce vibration and noise involves a variety of factors, with three main electromagnetic causes being addressed [4,5]. These sources are as follows. First, there is cogging torque due to changes in the reluctance of the stator slots as the rotor rotates [6–8]. Second, there is torque ripple as a result of the fifth and seventh harmonic components arising from the temporal and spatial harmonic components when current is applied [9–11]. Finally, there are radial and tangential forces that occur during rotation [12–14]. An international standard established in 1974 is the only standard that evaluates the vibration generated by electric motors and is shown in Table 1 [15,16]. This standard is divided into Class 1 through Class 4 depending on the capacity of the motor and is evaluated as four grades: A (good), B (slightly bad), C (bad), and D (extremely bad) based on the RMS value of the vibration speed generated in the motor housing. This study presents a theoretical study on the modification of rotor geometry to minimize vibration and noise at rated and maximum operating speeds for a 16-pole 24-slot traction motor [17,18]. The main objectives of the study are as follows. The first is to minimize vibration noise by applying tapering to the rotor core to minimize the cogging torque due to the change in reluctance of the stator slot with the rotation of the rotor. Second, an asymmetric two-step skew is applied to the tapered rotor by dividing the rotor into upper and lower parts to adjust the cogging torque and back electromotive force (EMF) to minimize vibration and noise. The RSM is used to derive the optimal model for cogging torque and vibration noise reduction [19–21]. To calculate the electromagnetic vibration in the proposed model, finite element analysis (FEA) with flux density analysis of the air gap is essential. In this process, the radial force, which is the source of the vibration, is obtained and the vibration velocity is predicted [22–25]. The results of these studies are verified using formulas and FEA, which will play an important role in improving the performance of electric motors as well as the convenience and satisfaction of users.

**Table 1.** Standard for the vibration grade ISO 2372 (ISO 10816-1).

<table>
<tr><th>RMS Vibration Velocity [mm/s]</th><th>Up to 15 [kW] Class I</th><th>15 to 75 [kW] Class II</th><th>>75 [kW] (Rigid) Class III</th><th>>75 [kW] (Soft) Class IV</th></tr>
<tr><td>0.28</td><td rowspan="3">A</td><td rowspan="4">A</td><td rowspan="5">A</td><td rowspan="6">A</td></tr>
<tr><td>0.45</td></tr>
<tr><td>0.71</td></tr>
<tr><td>1.12</td><td rowspan="2">B</td></tr>
<tr><td>1.8</td><td rowspan="2">B</td></tr>
<tr><td>2.8</td><td rowspan="2">C</td><td rowspan="2">B</td></tr>
<tr><td>4.5</td><td rowspan="2">C</td><td rowspan="2">B</td></tr>
<tr><td>7.1</td><td rowspan="5">D</td><td rowspan="2">C</td></tr>
<tr><td>11.2</td><td rowspan="4">D</td><td rowspan="2">C</td></tr>
<tr><td>18</td><td rowspan="3">D</td></tr>
<tr><td>28</td><td rowspan="2">D</td></tr>
<tr><td>45</td></tr>
</table>

Zone A: The vibration of a newly installed machine usually falls within this zone. Zone B: Machines that vibrate within this zone are generally considered to be acceptable for long-term operation without restrictions. Zone C: Machines that vibrate within this zone are generally considered unsatisfactory for long-term continuous operation. Zone D: Vibration values in this zone are generally considered to be severe enough to cause damage to the machine.

## 2. Theoretical Analysis

### *2.1. Analyze the Cause of Cogging Torque*

There have been countless studies and significant research on the causes of cogging torque. Cogging torque is an irregular torque that occurs when the rotor of an electric motor interacts with the stator. It interferes with the smooth rotation of the motor and causes vibration and noise. Cogging torque can be expressed as:

$$T_{cog} = -\frac{1}{2}\varnothing_m^2\frac{dR}{d\theta} \quad (1)$$

where $\varnothing_m$ represents the magnetic flux from a permanent magnet and the remaining term is the change in reluctance. Figure 1 shows an example of the geometry of how cogging torque occurs. As the rotor rotates, the magnetic flux from the permanent magnet tends to flow toward the side. The smaller reluctance is due to the difference in reluctance between the stator slot opening and the stator tooth, resulting in a change in reluctance and cogging torque. In this study, rotor tapering and a two-step skew were applied to reduce this change in reluctance.

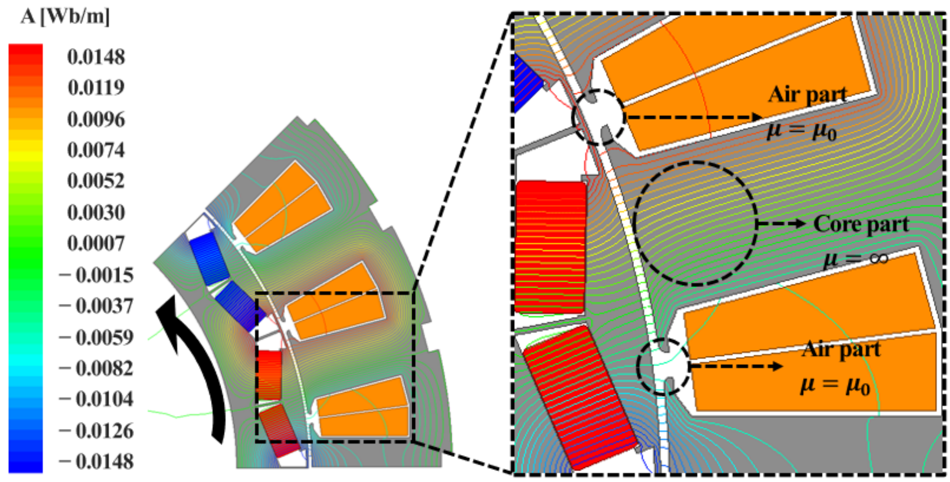


**Figure 1.** Example explanation of cogging torque occurrence.

## 2.2. *Analysis of Electromagnetic Vibration of Motor*

### 2.2.1. Electromagnetic Vibration Source (Radial Force)

Electromagnetic vibration is a radial force that propagates into the air. This is transmitted from the stator back to the housing, and the radial force that contributes to external noise can be calculated as the square of the air gap flux density. The torque density of an electric motor is proportional to the air gap flux density, and IPMSM types with higher torque densities exhibit greater electromagnetic vibration. In addition to electromagnetic performance, it is necessary to design an electric motor that considers vibration noise for high quality, and to do so, the basic design should consider not only torque, power, and efficiency, but also vibration caused by electromagnetic forces. Vibration velocity is the radial vibration speed generated by an electromagnetic radial force acting on the stator shoes or teeth and transmitted to the stator outer diameter. It can be expressed as vibration acceleration through differential calculation, but vibration velocity is used in this paper. In general, the radial force received in a unit area is equal to the square of the total flux density minus the square of the tangential component of the flux density [22–24]. The radial force is expressed as follows:

$$p(\theta^m, t) = \frac{1}{2\mu_0}\left[B^2(\theta^m, t) - B_t^2(\theta^m, t)\right] \cong \frac{1}{2\mu_0} B^2(\theta^m, t) \tag{2}$$

where $\theta$, $t$ are the components in space and time, $\mu_0$ is the permeability of the air gap, and $B(\theta^m, t)$, and $B_t^2(\theta^m, t)$ are the total and tangential air gap flux density. Since the permeability of the iron core is much higher than the permeability of the air gap, the flux path is almost perpendicular to the rotor and stator core. Therefore, the air gap flux density in the tangential direction can be neglected because it is a very small value compared to the radial direction. The flux density $B(\theta^m, t)$ in Equation (2) is the sum of the flux densities occurring in the stator and rotor windings and is equal to:

$$B(\theta^m, t) = B^s(\theta^m, t) + B^r(\theta^m, t) \tag{3}$$

By substituting Equation (3) into Equation (2), we derived the following expression, which can be expressed as:

$$\begin{aligned} p(\theta^m, t) &= \tfrac{1}{2\mu_0}\left[B^s(\theta^m, t) + B^r(\theta^m, t)\right]^2 \\ &= \tfrac{1}{2\mu_0}\left[\{B^s(\theta^m, t)\}^2 + 2\left\{B^s(\theta^m, t)B^r(\theta^m, t)\right\} + \{B^r(\theta^m, t)\}^2\right] \end{aligned} \tag{4}$$

Equation (4) is expressed in three parts: the radial force due to the flux density of the stator winding, the radial force due to the stator and rotor flux density, and the radial force due to the rotor flux density. If the current applied to the motor is assumed to be sinusoidal, which is an ideal condition, the time harmonic component of the stator flux density is only the fundamental wave component, and the rotor flux density generates harmonic components in addition to the fundamental wave.

#### 2.2.2. Stator System Mechanical Properties for Vibration Calculations

The electromagnetic vibration generated in the stator is influenced by the circumferential mode of the radial force, its frequency, and magnitude. Therefore, the radial force as a source of electromagnetic vibration must be separated into its circumferential modes and analyzed for quantitative and qualitative characteristics in terms of magnitude and frequency. In addition, the mechanical system must be taken into account to predict electromagnetic vibrations in motors. However, it is very difficult to make a perfect prediction of the vibration considering the mechanical structure. Therefore, assuming that the radial force affects the inner part of the stator, the shoe part, a simple model of the stator is used to analyze the vibration displacement and vibration velocity mathematically with some assumptions. First, the stator is assumed to be a ring-shaped cylinder, as shown in Figure 2. Since vibration velocity and vibration displacement are generated in the circumferential direction by the radial force, which is an electromagnetic force, it is necessary to find the vibration mode $m$ and the natural frequency of the stator system in the circumferential direction to analyze it.

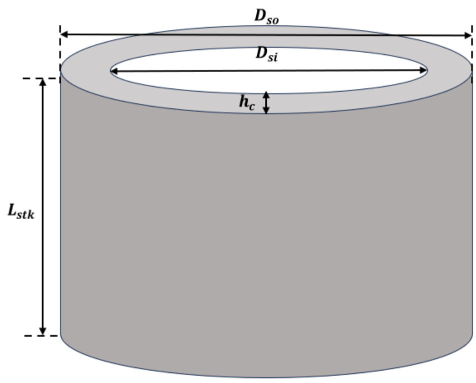


**Figure 2.** Simplified stator design.

The vibration displacement $A_m$ caused by the $m$th order vibration mode in the circumferential direction is expressed by the circumferential mode of the radial force with $r = m$, as shown in Equation (5):

$$A_m = \frac{F_m / M_c}{\sqrt{(\omega_m^2 - \omega_r^2)^2 + 4\zeta_m^2 \omega_r^2 \omega_m^2}} \tag{5}$$

where $M_c$ is the mass of the stator core [kg], $\omega_r$ is the angular frequency of the radial force, $\omega_m$, $\zeta_m$ are the natural frequency in mode $m$ and the damping ratio. The magnitude of the force experienced by the stator is then:

$$F_m = \pi D_{si} L_{stk} P_{mr} \tag{6}$$

where $D_{si}$ is the stator inner diameter, $L_{stk}$ is the stack length, and $P_{mr}$ is the magnitude of the radial force in mode $m$.

According to Equation (5), as the angular momentum $\omega_r$ of the radial force approaches the natural angular momentum $\omega_m$ of the mode m, the vibration becomes larger, and the vibration of the mode m is maximized when $\omega_r = \omega_m$. Reformulating Equation (5) with the magnification factor $h_m$, yields:

$$h_m = \frac{A_m}{F_m/(M_c\omega_m^2)} = \frac{1}{\sqrt{\left[1-(f_r/f_m)^2\right]^2 + [2\zeta_m(f_r/f_m)]^2}} \quad (7)$$

where $f_r$ is the vibration frequency of the $r$th order vibration mode and $f_m$ is the natural frequency of the mode $m$. As $\Delta f = |f_r - f_m|$ and the damping ratio $\zeta_m$ decrease, the magnification factor $h_m$ increases. Especially when $f_r = f_m$, the magnitude of the vibration depends on the mechanical damping of the device structure.

However, the mechanical damping ratio is often difficult to predict with a formula, so it is usually analyzed empirically through experiments. The empirical damping ratio is a practical approach to approximate complex mechanical damping that is difficult to describe theoretically. In small- and medium-sized electrical devices, it is used to express damping ratio as a function of frequency or other design variables based on experimental data to predict the dynamic behavior of the device and perform design and optimization. The empirical damping ratio for small- and medium-sized electrical devices is as follows [26]:

$$\zeta_m = \frac{1}{2\pi}\left(2.76 \times 10^{-5} f_m + 0.062\right) \quad (8)$$

From Equation (8), it can be concluded that as the natural frequency $f_m$ increases, the damping ratio $\zeta_m$ also increases. Equation (5) is the vibration displacement due to one mode, and to obtain the total vibration displacement, the vibration displacement due to all modes must be calculated. Assuming that the natural frequency of each mode is distributed in such a way that they do not affect other modes, the vibration displacement caused by each mode can be calculated by substituting the natural frequency of each mode into Equation (5). Reformulating Equation (5) with the previously obtained expressions for the magnitude of the radial force $P_{mr}$ and the magnification factor $h_m$, yields:

$$A_m = \frac{F_m}{M_c w_m^2} h_m = \frac{\pi D_{si} L_{stk}}{M_c \omega_m^2} P_{mr} h_m \quad (9)$$

Since radial force is a function of time and space, the velocity of vibration $V_m$ in mode $m$ is the derivative of $A_m$ with respect to time $t$. Therefore:

$$V_m = \omega_r A_m = 2\pi f_r \frac{\pi D_{si} L_{stk}}{M_c \omega_m^2} P_{mr} h_m \quad (10)$$

As shown in the above equation, the vibration displacement and vibration velocity are determined by the natural frequency $\omega_m$ and the magnification factor $h_m$. In addition, the natural frequency increases as the mode increases, so even if the magnitude of the radial force is the same, the effect of vibration is relatively small for higher-order modes, and conversely, the effect of vibration is large for lower-order modes.

#### 2.2.3. Calculate the Natural Frequency of the Stator

It is very important to calculate the natural frequency of a stator in order to predict the vibration generated by the stator. In general, the natural frequency of the stator is calculated by considering the stator configuration, considering the core, windings, housing, etc. In this section, the natural frequency of the stator is calculated by assuming the mechanical geometry of the stator is a ring-shaped cylinder, as shown in the previous assumption. In general, the mode-specific natural frequency of the stator is as follows:

$$f_m = \frac{1}{2\pi}\sqrt{\frac{K_m}{M_m}} \quad (11)$$

where $K_m$ is the stator stiffness in mode $m$ and $M_m$ is the stator mode mass. Therefore, the natural frequency $f_m$ in mode $m$ can be calculated by finding $K_m$ and $M_m$. In Equation (10), $r$ = 0, 1, 2, 3... represents the order of the circumferential mode and corresponds to the spatial harmonic component of the radial force, which has different effects on the vibration depending on the order of the circumferential mode. Figure 3 shows the results of 3D FEA modal analysis of the stator geometry, without the windings of the conventional model, conducted in this paper with Ansys Workbench, and the results for the modal geometries ($m$ = 2, $m$ = 3, $m$ = 4) were obtained. The material of the stator is Steel_1010, Young's modulus is 205 [GPa], Poisson's ratio is 0.28, and mass density is 7872 [kg/m$^3$]. The frequency of each circumferential mode obtained by modal analysis is relatively far away from the electrical frequencies of 2 fe (472 [Hz]), 4 fe (944 [Hz]), 6 fe (1416 [Hz]), and 8 fe (1888 [Hz]) of the conventional model, so there is less concern about resonance.

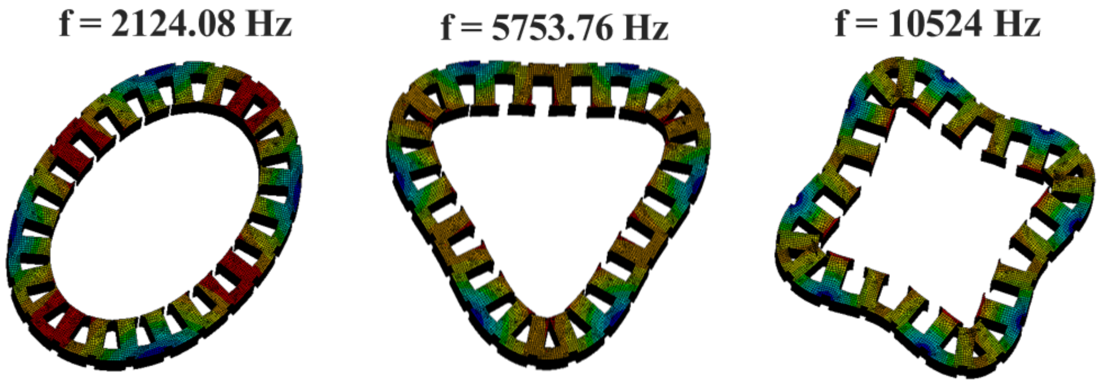


(**a**) (**b**) (**c**)

**Figure 3.** 3D FEA analysis results of natural frequency and corresponding modal shapes (**a**) $m$ = 2, (**b**) $m$ = 3, (**c**) $m$ = 4.

2.2.4. Extraction Main Vibration Factor Harmonics Order

The radial force and vibration velocity have different time/space harmonic components depending on the position as the rotor rotates. For the conventional model in this paper, there are 16 poles and 8 pole pairs. Therefore, the radial force and vibration velocity are dominated by the temporal harmonic order components of the second order and the spatial harmonic order components of the eighth order.

In the case of temporal harmonic order, radial force and vibration velocity are considered up to the 10th order of the 2nd multiple because of their significant influence. For the spatial harmonic order, the comparison was conducted in eight orders of magnitude from 0 to 56. Figure 4 shows a comparison of the magnitude of radial force and vibration velocity at the rated speed of the conventional model (1770 rpm) with each temporal and spatial harmonic order component. In Figure 4a, the $x$-axis shows the spatial harmonic order from the 0th to the 56th in multiples of 8, the corresponding temporal harmonic order from the 2nd to the 10th in multiples of 8, and the $y$-axis shows the corresponding radial force density. The radial force density values show the greatest influence at the 16th spatial harmonic order because the motor is 16 poles, and the influence decreases as the order increases.

In this paper, we needed to extract the order with time/space influence, so we analyzed the influence of vibration velocity based on the same time/space harmonics, as shown in Figure 4b. In Figure 4b, we can see that the zero-order spatial harmonic component of the vibration velocity is 0 [Hz], so it does not vibrate in the presence of radial force, so it is excluded from the harmonic order to be extracted. Figure 4a,b shows the extraction of the influential temporal and spatial harmonic orders. Table 2 analyzes the radial force and vibration velocity in time/space to extract the influential harmonic components. In this study, the radial force was analyzed through these extracted dominant harmonics [19].

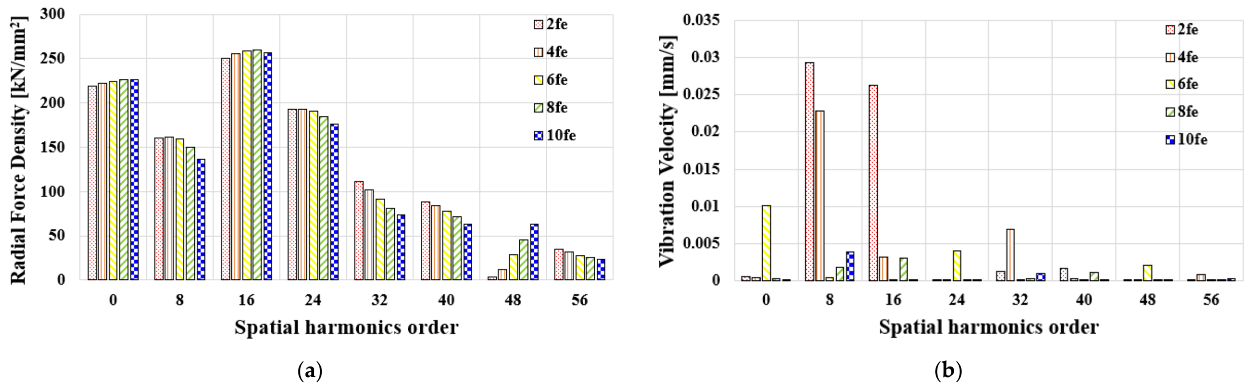


**Figure 4.** Time/spatial harmonic order separation of (**a**) the radial force density (**b**) the vibration velocity (@1770 rpm).

**Table 2.** Selected time/spatial harmonics order.

| | Time Harmonics Order | | | | |
|---|---|---|---|---|---|
| | **2 fe** | **4 fe** | **6 fe** | **8 fe** | **10 fe** |
| Spatial harmonics order | 8, 16, 32, 40 | 8, 16, 32, 56 | 0, 24, 48 | 8, 16 | 8, 32 |

## 3. Conventional Model Specifications

### *3.1. Analyze Conventional Model Electromagnetic Performance*

The conventional model selected in this paper is a 24[kW] traction motor, which is an IPMSM with 16 poles and 24 slots that uses a V-shaped rotor structure. The geometry of this motor was realized through Ansys MAXWELL 2024 R2 2D software, and the results are shown in Figure 5a. Since the model was too complex and difficult to analyze to include mechanical factors, the results were based on electromagnetic FEA. The meshing in the FEA is important to check the cogging torque and air gap flux density, so a more refined mesh was applied to the air gap between the stator and rotor. This resulted in a total mesh count of 17,320 elements in 2D. For the motor analysis, the nonlinearity problem, which takes into account the saturation component of the core and the demagnetization of the permanent magnet, was solved using the Newton-Raphson method with an energy convergence criterion to improve accuracy. Ansys MAXWELL 2024 R2 program was used as the analysis tool. To ensure the reproducibility and reliability of this FEA, the conventional model was referenced to the actual fabricated model [1], and the simulation results were verified by comparing them with the existing literature. This ensured the accuracy and reliability of the results.

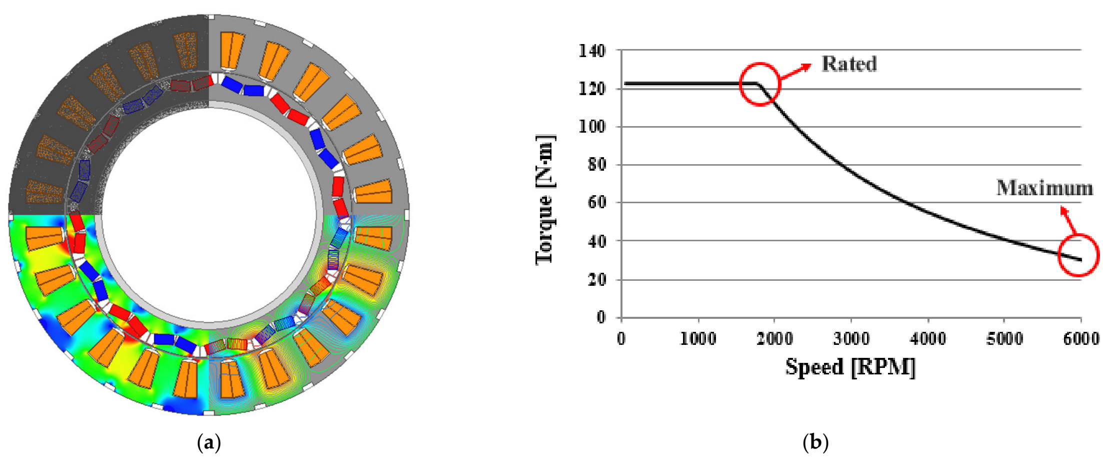


**Figure 5.** Conventional model (**a**) geometry (**b**) TN curve.

In addition, the torque-speed (TN) curve of this model is shown in Figure 5b. In this curve, the red circle on the left represents the rated operating condition at 1770 rpm and the red circle on the right represents the maximum operating condition at 6000 rpm. The major specifications for these two operating conditions are summarized in Table 3. For the rated and maximum operating conditions of the conventional model, referring to Equation (1), it can be seen that the amount of flux generated by the permanent magnets is constant, so the change in flux and reluctance is almost the same. This also maintains the cogging torque constant at 10.4 [N·m], which means that since there is no change in the rotor geometry, the reluctance remains constant and there is no significant difference in the cogging torque.

**Table 3.** Conventional model basic specifications.

| Parameter | 1770 rpm | 6000 rpm | Unit |
|---|---|---|---|
| Stator & Rotor | Steel_10101 | | - |
| Coil | Copper | | - |
| Magnet | N42UH | | - |
| Pole/Slot | 16/24 | | - |
| Stator outer diameter | 280 | | mm |
| Rotor outer diameter | 200 | | mm |
| No-load phase back EMF | 76.8 | 260.4 | $V_{rms}$ |
| Cogging torque | 10.4 | 10.4 | N·m |
| Current | 102.5 | | $A_{rms}$ |
| Torque | 128 | 26.3 | N·m |
| Line Back EMF | 202.9 | 205.5 | V |
| Output | 23.6 | 16 | kW |
| Efficiency | 96.8 | 85.9 | % |

### *3.2. Analyze Conventional Model Vibration*

The vibration noise characteristics were analyzed under the rated (1770 rpm) and maximum (6000 rpm) operating conditions of the conventional model. Figure 6 shows the electromagnetic characteristics at the initial position ($\omega t$ = 0) extracted by 2D FEA for vibration noise prediction. Figure 6a shows the flux density as a function of mechanical position at rated and maximum operation from the conventional model. Figure 6b is a radial graph of the radial force [kN/mm$^2$] at a specific position ($\omega t$ = 0). The spatial harmonics are difficult to match perfectly because the rotational speed contains multiple temporal harmonics.

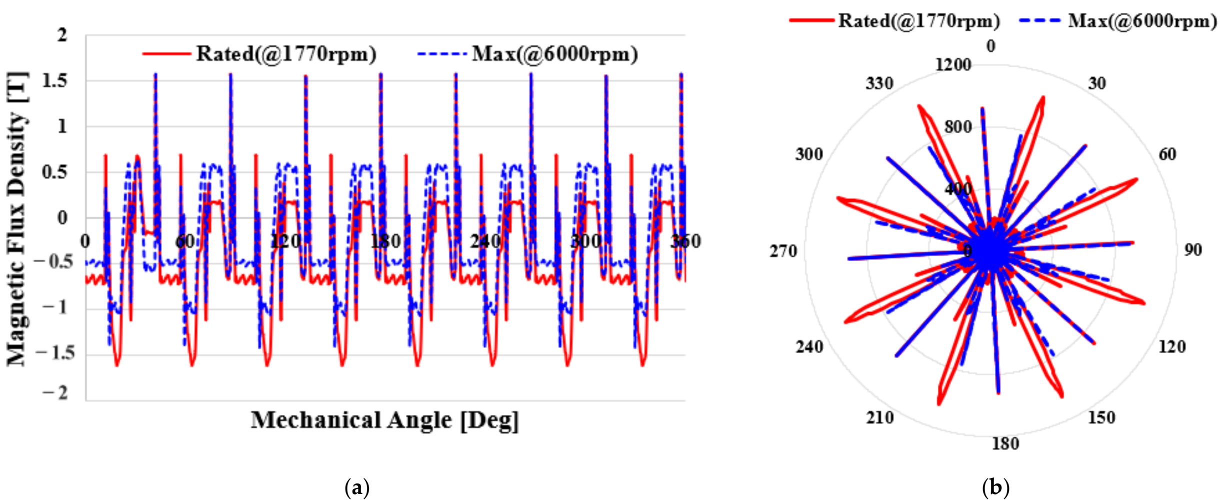


**Figure 6.** Electromagnetic characterization of conventional models with 2D FEA ($\omega t$ = 0) (**a**) magnetic flux density (**b**) radial force density [kN/mm$^2$].

Figure 7 shows the results of deriving the vibration noise characteristics from the temporal and spatial harmonic components extracted through 2D FEA. In Figure 7a, the

$x$-axis lists the spatial harmonic order extracted from each temporal harmonic component, which is used to compare the radial force density. Since the model has 16 poles, we can see that the largest values are found mainly at the 8th and 16th orders. The radial force density at the rated condition (1770 rpm) is larger than the maximum condition (6000 rpm), which is due to the fact that the beta angle control at maximum operation tends to generate a reverse magnetic field, resulting in a lower radial force density. Figure 7b shows a comparison of the vibration velocity for each time harmonic order. Since the zero-order time harmonic component is 0 [Hz], it can be seen that the presence of radial forces does not cause vibration. The vibration velocity RMS value at rated is 0.52 [mm/s], and at maximum condition, it is 2.94 [mm/s], which is higher than the rated value. This was analyzed as a result of the increase in vibration velocity due to the increase in speed and frequency during maximum operation.

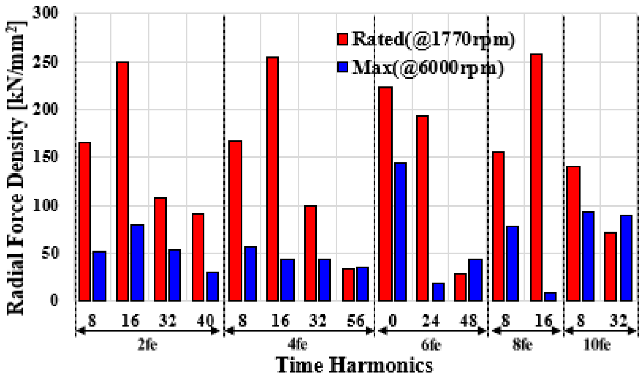


(**a**)

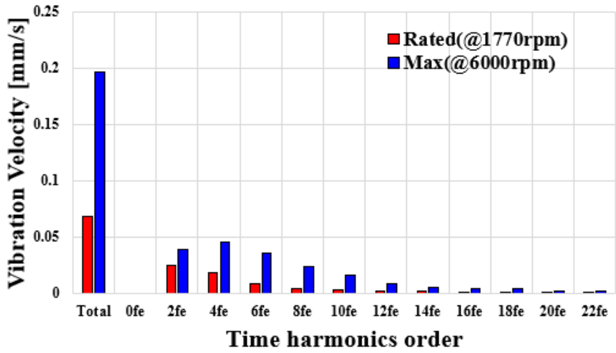


(**b**)

**Figure 7.** Comparison of conventional model electromagnetic characterization at rated speed (1770 rpm) and maximum speed (6000 rpm) (**a**) and the radial force density distribution over the selected time/space harmonic order. Overall, higher radial force at rated operation than at maximum operation, (**b**) comparison of vibration rates for different harmonic orders. For the overall harmonic order, the vibration velocity is lower at rated operation than at maximum operation, with a significant increase in total vibration velocity at maximum operation.

## 4. Proposed Model

### *4.1. Main Variable Parameters*

Figure 8 shows the rotor tapering parameters tapering thickness ($T_t$) and tapering angle ($T_{deg}$). $T_t$ suggests tapering at the rib so as not to obstruct the flow of magnetic flux from the permanent magnet.

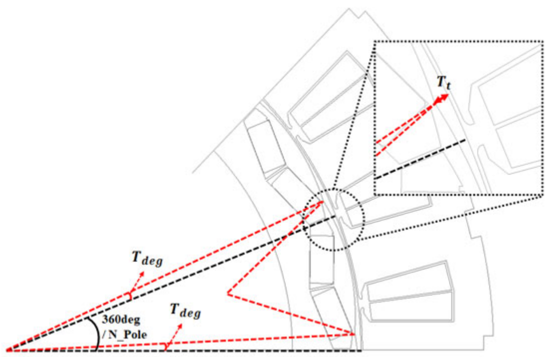


**Figure 8.** Definition of $T_t$, $T_{deg}$.

For manufacturability considerations, the length of $T_t$ is formed such that the rib thickness is at least 0.6 [mm]. To reduce the effect on the back EMF, $T_{deg}$ is given to the rib area, except the pole piece area where the main magnetic flux flows, to provide an ideal cogging torque reduction model. When applying the variable of $T_{deg}$, a two-step skew is applied by dividing the stack length in half and angling it in opposite directions while keeping $T_t$ applied. This has the effect of canceling out cogging torque in any localized area subjected to a difference in reluctance.

### *4.2. Deriving the Optimal Model*

In this paper, to perform optimal design using the variables in Figure 8, we used the response surface method (RSM), which can statistically analyze the influence of a response variable on multiple variables to derive an optimal model. In this paper, we considered the optimal design of the objective function using two variables. Based on a comprehensive consideration of the suitability, complexity, and compatibility with the experimental design of optimal design methods, we conclude that RSM provides an interpretable and simplified optimization approach compared to other methods. In particular, the second-order polynomial regression model is used as a mathematical tool to clearly represent the interaction between variables and effectively solve the optimization problem [27,28]. RSM is a method that statistically analyzes the change in response when multiple variables $X$ act in combination to affect a specific response variable $Y$ [19,20]. The experimental range of the proposed variables for the conventional model at rated operation (1770 rpm) is shown in Table 4. Equation (12) shows the fundamental equation of the second-order polynomial regression function, and Equations (13)–(15) show the regression functions for cogging torque, no-load back EMF, and vibration velocity, respectively.

$$y_i = \beta_0 + \sum_{i=1}^{p} \beta_i x_i + \sum_{i \leq j}^{p} \beta_{ij} x_i x_j + \varepsilon_i \tag{12}$$

$$y_{Cogging\ torque} = 4.49 - 4.12(X_1) - 0.65(X_2) \cdots - 0.73(X_1)(X_2) \tag{13}$$

$$y_{Noload\ back\ EMF} = 73.9 - 2.16(X_1) - 2.24(X_2) \cdots - 1.96(X_1)(X_2) \tag{14}$$

$$y_{Vibration\ velocity} = 0.39 - 0.11(X_1) - 0.02(X_2) \cdots - 0.02(X_1)(X_2) \tag{15}$$

where $\beta_1, \beta_2, \cdots, \beta_k$ are the regression coefficients of each variable, $x_1, x_2, \cdots, x_k$ are the variables in the code, $\varepsilon$ is the error term in the response, and $X_1 - X_2$ are the variables $T_t$, $T_{deg}$. Table 4 shows the ranges of design variables set to use RSM. Variable $T_t$ was set to 0–1.8 [mm] to account for a minimum fabrication thickness of 0.6 [mm] and a range of no more than 1.8 [mm] without physically destroying the rotor geometry. Variable $T_{deg}$ was set to 0–3.0[°], considering the range from the pole piece to the rib piece, excluding the area that does not affect the pole piece, which is the passage through which the main magnetic flux flows, while maintaining the same performance to the extent possible. Subsequently, the variables were selected based on the design of experiments (DoE) method, which systematically selects experimental variables and value ranges for optimal design. Based on the variables and ranges presented in Table 4, a design matrix including center points (0.9 [mm], 1.5[°]) and axis points (1.8 [mm], 3.0[°], etc.) was generated using a quadratic response surface method design and central composite design (CCD). The optimized increment size was then set, and the optimization was performed by substituting the optimal points derived from the RSM into the regression function, and the optimal points were derived as $T_t$ = 1.8 [mm] and $T_{deg}$ = 3.0[°]. Comparing RSM and FEA, we found that the error was less than 1[%]. The error rate was similar to the FEA results, which is enough to prove its effectiveness and reliability. The reason for the slight error is that the CCD was used to derive the optimal model based on the design matrix including the center and axis points. If the sampling points were set more precisely, the error rate in certain areas would be significantly reduced.

**Table 4.** Design variables and experiment range for RSM.

| Contents | $T_t$ [mm] | $T_{deg}$ [°] |
|---|---|---|
| Range | 0–1.8 | 0–3.0 |
| Optimal point | 1.8 | 3.0 |

In conclusion, we can conclude that RSM is valid. The results of the RSM results are shown in Figures 9 and 10, where the estimated values are plotted against the variables $T_t$ and $T_{deg}$. Figure 9a shows the cogging torque at the rated speed of 1770 rpm, and it can be seen that the larger the values of $T_t$ and $T_{deg}$, the smaller the reluctance change, which reduces the cogging torque. Figure 9b shows the no-load back EMF, and it can be seen that as $T_t$ and $T_{deg}$ become larger, the polypiece portion, which is the magnetic flux path, shrinks, resulting in a proportional decrease in the back EMF. Figure 9c shows the RMS vibration velocity, and, similar to the cogging torque, it can be seen that the vibration velocity decreases as $T_t$ and $T_{deg}$ increase. In this paper, it was determined that the conventional model can maintain the same performance even if the no-load back EMF is slightly reduced because the current density has a margin of about 10%. Therefore, the final model is proposed by selecting the optimum point of $T_t = 1.8$ [mm], $T_{deg} = 3.0$[°]. Figure 10 shows the results of each variable at the maximum operating speed of 6000 rpm, and the optimum model is derived in a similar way to Figure 9.

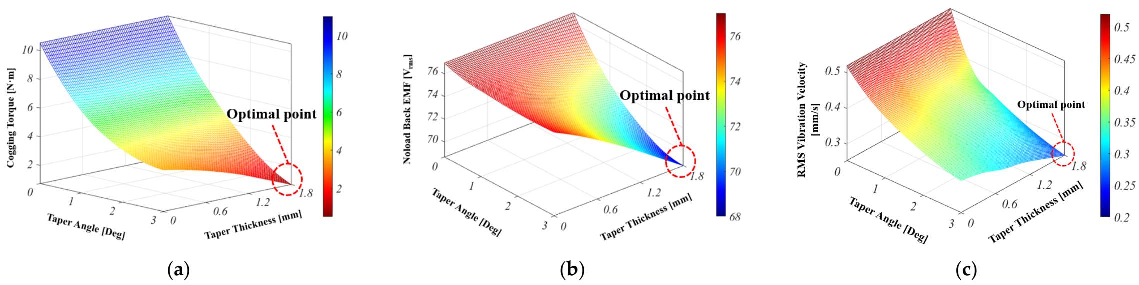


**Figure 9.** Results of deriving response variables based on variables a and b with RSM (rated @1770 rpm) (**a**) cogging torque (**b**) no-load back EMF (**c**) RMS vibration velocity.

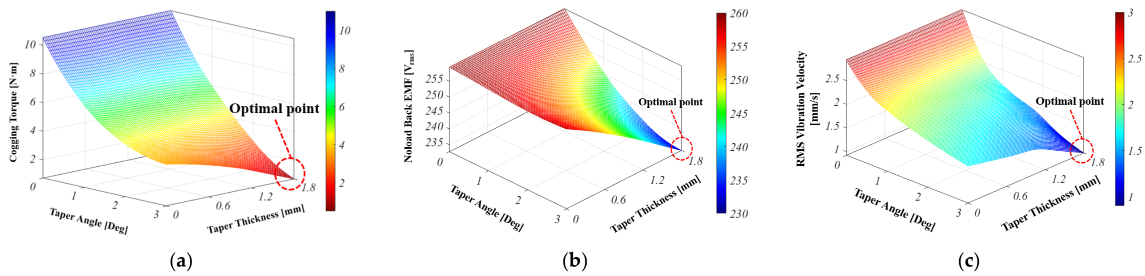


**Figure 10.** Results of deriving response variables based on variables a and b with RSM (max @6000 rpm) (**a**) cogging torque (**b**) no-load back EMF (**c**) RMS vibration velocity.

### *4.3. Comparative Analysis of Proposed Model Performance Characteristics*

#### 4.3.1. Electromagnetic Performance of Proposed Model

As explained earlier, the optimal proposed model with $T_t = 1.8$ [mm], $T_{deg} = 3.0$[°] was derived through RSM. As a result, the proposed rotor two-step skew geometry reduces the cogging torque by about 91.6[%] at nominal and about 91.8[%] at maximum compared to the conventional model while maintaining the same performance even though the no-load back EMF is slightly reduced. Figure 11a shows the 3D realization of the 1/8th cycle model of the conventional model rotor. Applying an asymmetric two-step skew to the rotor in the conventional model results in the geometry shown in Figure 11b. The waveforms of cogging torque and no-load back EMF are shown in Figure 12. Figure 12a shows that the total cogging torque can be canceled out in both sections through the asymmetric angle at the top and bottom, which reduces the cogging torque. Figure 12b shows that the asymmetric structure of the rotor at the top and bottom prevents the asymmetric structure of the back EMF, which enables the maximum back EMF and maximum torque.

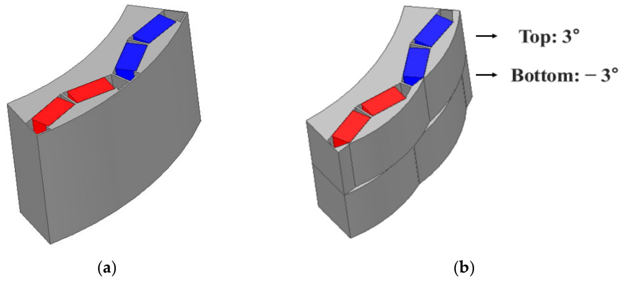


**Figure 11.** Model topology (**a**) conventional model (**b**) proposed model.

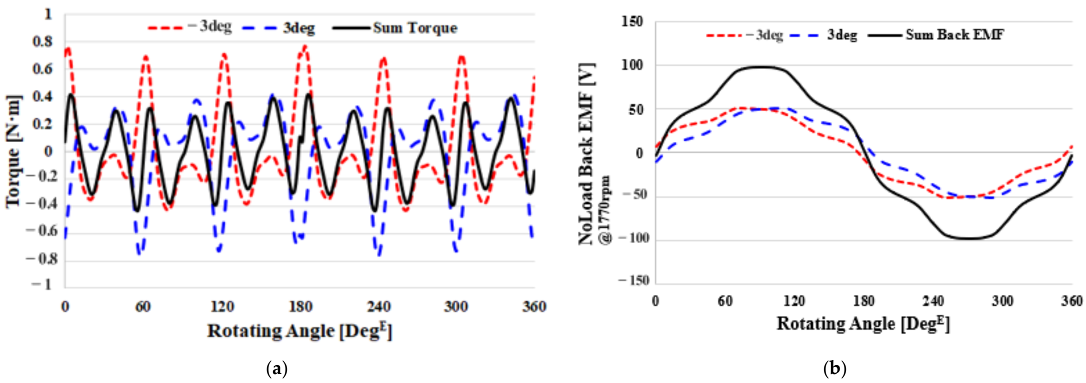


**Figure 12.** Sum waveform according to $T_{deg} = 3.0[°], -3.0[°]$ (**a**) cogging torque (**b**) no-load back EMF(@1770 rpm).

To determine the mechanical safety of the proposed model, Workbench 3D FEA was performed at maximum operation (6000 rpm) and the results are shown in Figure 13. Figure 13a shows the equivalent stress of the proposed model. Here, the maximum stress is generated locally between the permanent magnet and the rib due to centrifugal force as the rotor rotates. However, the analysis shows that the yield tensile strength of Steel_1010 is 78.45 [MPa], compared to 18.05 [MPa], which is low enough to be mechanically robust. Figure 13b also shows that the minimum safety factor is about 4.4. As an empirical value, a safety factor of 2 or more is considered safe. Therefore, the proposed model can be said to be mechanically robust at rated and maximum operation.

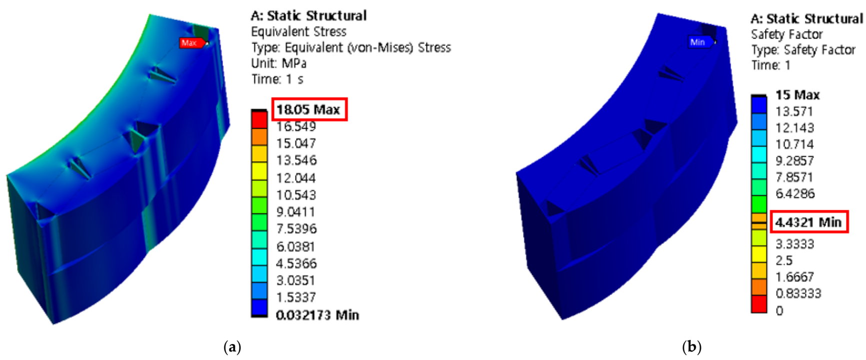


**Figure 13.** Result of mechanical stiffness analysis of the proposed model (**a**) equivalent stress, (**b**) minimum safety factor.

#### 4.3.2. Electromagnetic Vibration Analysis

To validate whether the radial force and vibration noise are substantially reduced by reducing the cogging torque, one of the electromagnetic vibration noise sources, a comparative analysis of the extracted main temporal and spatial harmonic order components was performed. Figure 14 shows the analysis of radial force and vibration velocity at a rated speed of 1770 rpm. Figure 14a shows the radial force values from the extracted time/space harmonic components. Compared to the conventional model, it was observed that the radial force is reduced overall in each harmonic component by the proposed model. In Figure 14b, the vibration velocity tends to decrease overall from the conventional model to the proposed model, which verifies that the proposed model reduces the vibration noise by about 51.9[%] compared to the conventional model at the rated level. The analysis of radial force and vibration velocity at the maximum operating speed of 6000 rpm using the same method is shown in Figure 15. In Figure 15a, the radial force tends to decrease overall when the proposed model is applied from the conventional model to the proposed model, but there are some sections where the value increases, which is partly due to the phenomenon that the vacancy flux density is temporarily skewed due to the saturation of both ribs, resulting in a partial increase at high spatial harmonic orders. However, in Figure 15b it can be seen that the vibration velocity is significantly reduced from the conventional model to the proposed model, and even if the radial force is increased at some spatial harmonic orders, it is judged that the vibration is also reduced because it is reduced overall. In other words, at the maximum, the vibration of the proposed model is reduced by about 68.7[%] compared to the conventional model. By reducing the cogging torque, it was possible to reduce the radial force, which ultimately reduced the vibration noise. As a result, Table 5 shows that applying the proposed model to the conventional model reduces the cogging torque and vibration velocity at rated and maximum operation.

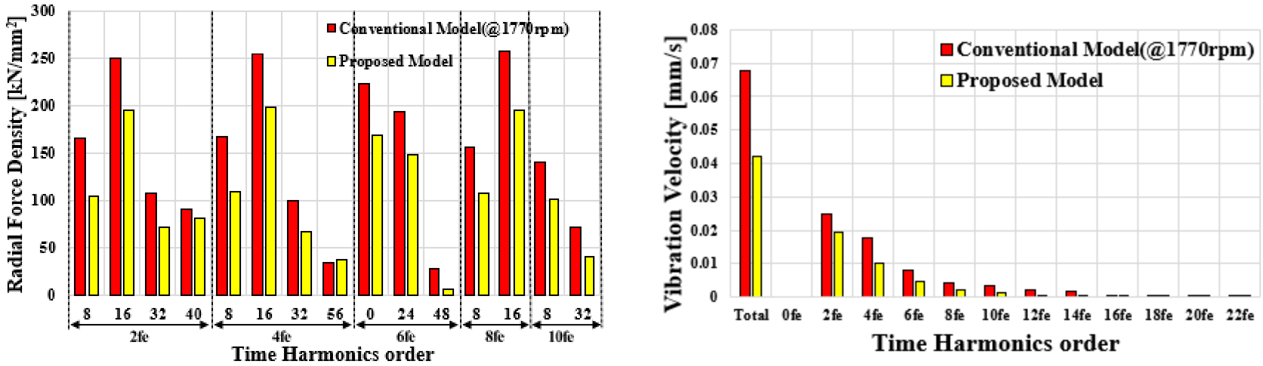


(**a**) (**b**)

**Figure 14.** Comparison analysis between the conventional and proposed models at the rated speed of 1770 rpm (**a**) the radial force density distribution over the selected time/space harmonic order. Overall lower radial force in the proposed model compared to the conventional model, which contributes to reduced vibration, (**b**) comparison of vibration rates for different harmonic orders. The proposed model reduces the total vibration velocity by reducing the overall harmonic order compared to the conventional model.

**Table 5.** Analyzed major results of the proposed model compared to the conventional model.

| Contents | Conventional Model | | Proposed Model | | Unit |
|---|---|---|---|---|---|
| | Rated 1770 rpm | Max 6000 rpm | Rated 1770 rpm | Max 6000 rpm | |
| Cogging torque | 10.4 | | 0.7 | | N·m |
| No-load back EMF | 76.8 | 260.4 | 68.7 | 232.8 | $V_{rms}$ |
| RMS vibration velocity | 0.52 | 2.94 | 0.25 | 0.92 | mm/s |

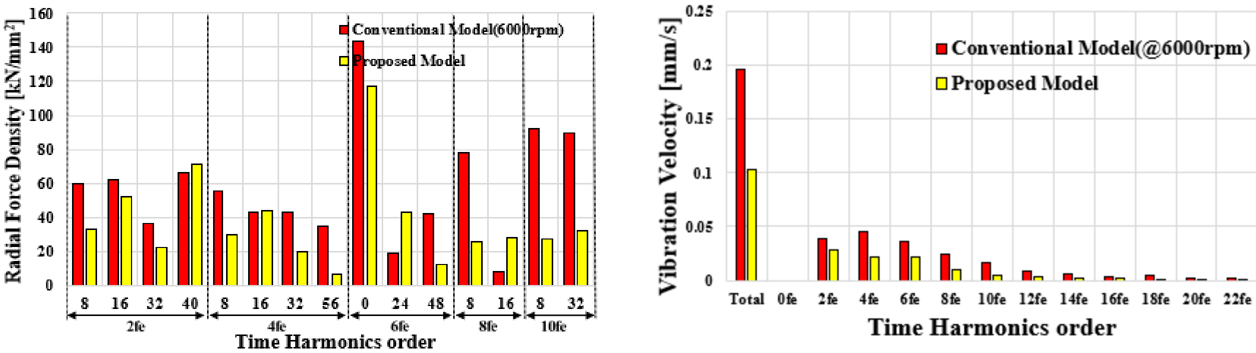


(**a**) (**b**)

**Figure 15.** Comparison analysis between the conventional and proposed models at the maxed speed of 6000 rpm (**a**) the radial force density distribution over the selected time/space harmonic order. Overall lower radial force in the proposed model compared to the conventional model, which contributes to reduced vibration, (**b**) comparison of vibration rates for different harmonic orders. The proposed model reduces the total vibration velocity by reducing the overall harmonic order compared to the conventional model.

## 5. Conclusions

The vibration and noise reduction proposal for traction motors proposed in this paper applies an asymmetric two-step skew model to the rotor to reduce the variation of magnetic resistance, resulting in a significant reduction of cogging torque. This approach significantly reduces cogging torque as well as vibration noise, contributing to improved operator comfort and minimizing negative impacts on the performance and lifetime of the motor. The reduction in cogging torque was significantly reduced to approximately 91.6[%] and 91.8[%] at rated and full operation, respectively. In addition, the vibration velocity was also reduced by approximately 51.9[%] at rated operation and 68.7[%] at full operation due to the overall reduction in radial force, as determined by extracting the dominant time/space harmonic components and identifying the corresponding radial force. The validity of the proposed model is demonstrated through formulations and FEA based entirely on numerical analysis and results.

**Author Contributions:** Conceptualization, S.-H.L. and S.-W.S.; Methodology, S.-H.L., S.-W.S. and W.-H.K.; Validation, S.-H.L., J.L. and W.-H.K.; Formal analysis, S.-H.L. and S.-W.S.; Investigation, S.-H.L., S.-W.S. and I.-J.Y.; Resources, I.-J.Y.; Data curation, I.-J.Y. and J.L.; Writing—original draft, S.-H.L. and I.-J.Y.; Writing—review & editing, S.-H.L.; Supervision, S.-W.S., J.L. and W.-H.K.; Project administration, J.L. and W.-H.K. All authors have read and agreed to the published version of the manuscript.

**Funding:** This work was partly supported by the Korea Institute of Energy Technology Evaluation and Planning (KETEP) grant funded by the Korean government (MOTIE) (20214000000060, Department of Next Generation Energy System Convergence Based on Techno-Economics—STEP). In part, this research was funded by the Energy Demand Management Core Technology Development Project (Development and Demonstration of Medium-sized Constant Speed High-Efficiency Electric Motors, No. RS-2023-00232767), funded by the Ministry of Trade, Industry, and Energy, and supported by the Korea Energy Technology Evaluation Institute (KETEP).

**Data Availability Statement:** The original contributions presented in the study are included in the article, further inquiries can be directed to the corresponding author.

**Conflicts of Interest:** The authors declare no conflicts of interest.

## References

1. Song, S.-W.; Kim, W.-H.; Lee, J.; Jung, D.-H. Design to Reduce Cogging Torque and Irreversible Demagnetization in Traction Hybrid Motor Using Dy-free Magnet. *Machines* **2023**, *11*, 345. [CrossRef]

2. Song, P.; Li, W.; Li, Z.; Toulabi, M.S.; Kar, N.C. Noise and Vibration Prediction of a Six-Phase IPMSM in a Single Open-Phase Failure Under a Negative Sequence Current Compensated Fault Tolerant Control Mode. *IEEE Trans. Magn.* **2022**, *58*, 1–6. [CrossRef]
3. Lin, F.; Zuo, S.G.; Deng, W.Z.; Wu, S.L. Reduction of vibration and acoustic noise in permanent magnet synchronous motor by optimizing magnetic forces. *J. Sound Vibr.* **2018**, *429*, 193–205. [CrossRef]
4. Gieras, A.; Jacek, F. *Noise of Polyphase Electric Motors*; Taylor & Francis CRC Press: Boca Raton, FL, USA, 2006.
5. Hartani, K.; Miloud, Y.; Miloudi, A. Improved direct torque control of permanent magnet synchronous electrical vehicle motor with proportional-integral resistance estimator. *J. Electr. Eng. Technol.* **2010**, *5*, 451–461. [CrossRef]
6. Wang, S.; Li, H. Reduction of Electromagnetic Vibration and Noise in Permanent Magnet Motor for EVs by Optimizing Design of Rotor Based on GPR-PSO Model. *J. Electr. Eng. Technol.* **2020**, *15*, 1231–1243. [CrossRef]
7. Park, Y.-W.; Ko, J.-S.; Kim, D.-K. Optimal Design of Step-Sloping Notches for Cogging Torque Minimization of Single-Phase BLDC Motors. *Energies* **2021**, *14*, 7104. [CrossRef]
8. Jo, I.-H.; Lee, H.-W.; Jeong, G.; Ji, W.-Y.; Park, C.-B. A Study on the Reduction of Cogging Torque for the Skew of a Magnetic Geared Synchronous Motor. *IEEE Trans. Magn.* **2019**, *55*, 1–5. [CrossRef]
9. Du, Z.S.; Lipo, T.A. High Torque Density and Low Torque Ripple Shaped-Magnet Machines Using Sinusoidal Plus Third Harmonic Shaped Magnets. *IEEE Trans. Ind. Appl.* **2019**, *55*, 2601–2610. [CrossRef]
10. Adase, L.A.; Alsofyani, I.M.; Lee, K.-B. Predictive Torque Control with Simple Duty-Ratio Regulator of PMSM for Minimizing Torque and Flux Ripples. *IEEE Access* **2020**, *8*, 2373–2381. [CrossRef]
11. Zhao, J.; Quan, X.; Tong, X.; Lin, M. Cogging Torque Reduction in Double-Rotor Hybrid Excited Axial Switched-Flux Permanent Magnet Machine. *IEEE Trans. Appl. Supercond.* **2020**, *30*, 1–5. [CrossRef]
12. Liu, N.-W.; Hung, K.-Y.; Yang, S.-C.; Lee, F.-C.; Liu, C.-J. Design of High-Speed Permanent Magnet Motor Considering Rotor Radial Force and Motor Losses. *Energies* **2020**, *13*, 5872. [CrossRef]
13. Jang, D.; Chang, J. Effects of Flux Modulation Poles on the Radial Magnetic Forces in Surface-Mounted Permanent-Magnet Vernier Machines. *IEEE Trans. Magn.* **2017**, *53*, 1–4. [CrossRef]
14. Hong, J.; Zhao, K.; Gui, L.; Cao, J. A Comprehensive Investigation of Tangential Force and Radial Force in PM Motor. *IEEE Trans. Ind. Electron.* **2024**, *71*, 16286–16296. [CrossRef]
15. *ISO 2372*; Mechanical Vibration of Machines with Operating Speeds from 10 to 200 rev/s—Basis for Specifying Evaluation Standards. ISO: Geneva, Switzerland, 1974.
16. *ISO 10816-1*; Mechanical Vibration—Evaluation of Machine Vibration by Measurements on Non-Rotating Parts—Part 1: General Guidelines. ISO: Geneva, Switzerland, 1995.
17. Zhang, G.; Hou, P. Optimization Design of Cogging Torque for Electric Power Steering Motors. *Machines* **2024**, *12*, 517. [CrossRef]
18. Chen, W.; Ma, J.; Wu, G.; Fang, Y. Torque Ripple Reduction of a Salient-Pole Permanent Magnet Synchronous Machine with an Advanced Step-Skewed Rotor Design. *IEEE Access* **2020**, *8*, 118989–118999. [CrossRef]
19. Yao, L.; Shen, J.-X.; Wang, Y.; Shi, D. Fast Prediction and Staged Optimization of Electromagnetic Vibration in Permanent Magnet Synchronous Motor. *IEEE Trans. Ind. Electron.* **2024**, *71*, 115–125. [CrossRef]
20. Siddique, F.; Singh, B.; Shastri, S. RSM Assisted MOGA for SRM EV Drive Control Factors Optimization. *IEEE Trans. Ind. Appl.* **2024**, *60*, 3200–3209. [CrossRef]
21. Calderón-Ramírez, M.; Gómez-Náfate, J.A.; Rico-Martínez, R.; Rodríguez-Castro, R.; Bravo-Sánchez, M.G.; Alcaraz-Caracheo, L.A. Improvement of Ohmic Pasteurization in Mango Pulp Through CFD and RSM. *IEEE Access* **2022**, *10*, 81380–81389. [CrossRef]
22. Lu, Y.; Li, J.; Yang, K. A Hybrid Calculation Method of Electromagnetic Vibration for Electrical Machines Considering High-Frequency Current Harmonics. *IEEE Trans. Ind. Electron.* **2022**, *69*, 10385–10395. [CrossRef]
23. Liang, J.; Jiang, J.; Callegaro, A.; Bilgin, B.; Dong, J.; Reeves, D.; Emadi, A. Prediction of Acoustic Noise and Vibration of a 24/16 Traction Switched Reluctance Machine. IET Electr. *Syst. Transp.* **2020**, *10*, 35–43.
24. Dong, Q.; Liu, X.; Qi, H.; Zhou, Y. Vibro-acoustic prediction and evaluation of permanent magnet synchronous motors. *Proc. Inst. Mech. Eng. Part D J. Automob. Eng.* **2020**, *234*, 2783–2793. [CrossRef]
25. Ibrahim, I.; Silva, R.; Mohammadi, M.H.; Ghorbanian, V.; Lowther, D.A. Surrogate-Based Acoustic Noise Prediction of Electric Motors. *IEEE Trans. Magn.* **2020**, *56*, 1–4. [CrossRef]
26. Yang, S.J. *Low-Noise Electrical Motors*; Clarendon Press: Oxford, UK, 1981.
27. You, Y.-M. Multi-Objective Optimal Design of Permanent Magnet Synchronous Motor for Electric Vehicle Based on Deep Learning. *Appl. Sci.* **2020**, *10*, 482. [CrossRef]
28. Sun, X.; Shi, Z.; Lei, G.; Guo, Y.; Zhu, J. Multi-Objective Design Optimization of an IPMSM Based on Multilevel Strategy. *IEEE Trans. Ind. Electron.* **2021**, *68*, 139–148. [CrossRef]